LIVERPOOL JOHN MOORES UNIVERSITY

LJMU Research Online

Carta, G, Jones, IS, Movchan, NV and Movchan, AB

Wave Characterisation in a Dynamic Elastic Lattice: Lattice Flux and Circulation

http://researchonline.ljmu.ac.uk/id/eprint/10881/

Article

Citation (please note it is advisable to refer to the publisher's version if you intend to cite from this work)

Carta, G, Jones, IS, Movchan, NV and Movchan, AB (2019) Wave Characterisation in a Dynamic Elastic Lattice: Lattice Flux and Circulation. Physical Mesomechanics, 22 (2). pp. 152-163. ISSN 1029-9599

LJMU has developed **LJMU Research Online** for users to access the research output of the University more effectively. Copyright © and Moral Rights for the papers on this site are retained by the individual authors and/or other copyright owners. Users may download and/or print one copy of any article(s) in LJMU Research Online to facilitate their private study or for non-commercial research. You may not engage in further distribution of the material or use it for any profit-making activities or any commercial gain.

The version presented here may differ from the published version or from the version of the record. Please see the repository URL above for details on accessing the published version and note that access may require a subscription.

For more information please contact researchonline@ljmu.ac.uk

http://researchonline.ljmu.ac.uk/

Wave characterisation in a dynamic elastic lattice: lattice flux and circulation

G. Carta[a], I. S. Jones[a], N. V. Movchan[b], A. B. Movchan[b,*]

[a] *Liverpool John Moores University, Mechanical Engineering and Materials Research Centre, Liverpool, L3 3AF, UK*
[b] *University of Liverpool, Department of Mathematical Sciences, Liverpool, L69 7ZL, UK*

Abstract

A novel characterisation of dispersive waves in a vector elastic lattice is presented in the context of wave polarisation. This proves to be especially important in analysis of dynamic anisotropy and standing waves trapped within the lattice. The operators of lattice flux and lattice circulation provide the required quantitative description, especially in cases of intermediate and high frequency dynamic regimes. Dispersion diagrams are conventionally considered as the ultimate characteristics of dynamic properties of waves in periodic systems. Generally, a waveform in a lattice can be thought of as a combination of pressure-like and shear-like waves. However, a direct analogy with waves in the continuum is not always obvious. We show a coherent way to characterise lattice waveforms in terms of so-called lattice flux and lattice circulation. In the long wavelength limit, this leads to well-known interpretations of pressure and shear waves. For the cases when the wavelength is comparable with the size of the lattice cell, new features are revealed which involve special directions along which either lattice flux or lattice circulation is zero. The cases of high frequency and wavelength comparable to the size of the elementary cell are considered, including dynamic anisotropy and dynamic neutrality in structured solids.

Keywords: Elastic waves, Lattice structures, Dynamic anisotropy, Lattice flux and circulation

In memory of Professor G.I. Barenblatt

1. Introduction

Scaling laws and asymptotic analysis are of great importance in mathematical modelling of physical phenomena, as described in fundamental monographs

*Corresponding author
Email addresses: g.carta@ljmu.ac.uk (G. Carta), i.s.jones@ljmu.ac.uk (I. S. Jones), nvm@liverpool.ac.uk (N. V. Movchan), abm@liverpool.ac.uk (A. B. Movchan)

[1–4]. Important examples include boundary layer fluid flow, reaction-diffusion problems and fracture, especially fracture in structured media. In particular, an elastic lattice represents a simple example of a structured solid, where propagation of cracks brings qualitatively new features compared to the continuum models, as discussed in [5–8]. Asymptotic analysis of structured solids has led to the well-developed approach of homogenisation, which is highly efficient in static problems [9–12]. Dynamic homogenisation, and in particular dynamic anisotropy of certain standing waveforms, was systematically studied in [13–15]. In dynamics a lattice, which would be considered as isotropic in a static homogenised state, displays new features associated with wave dispersion and dynamic anisotropy (see, for example, [16, 17]). Green's functions in dynamic lattices versus homogenisation approximations were considered in [18]. In recent years, the questions of polarisation of elastic waves in lattice systems and dynamic anisotropy were also raised in [19–23].

For a general periodic elastic lattice, the dispersion diagram is conventionally considered as the ultimate characteristic of the dynamic properties of waves in such a system. However, if one is interested in the combination of pressure and shear in a particular lattice waveform, the answer is not always obvious. The present paper shows a coherent way to characterise lattice waveforms in terms of so-called lattice flux and lattice circulation. Of course, in the long wavelength limit, this leads to well-known interpretations of pressure and shear waves. However, for the cases when the wavelength is comparable with the size of the lattice cell, new features are revealed which involve special directions along which either lattice flux or lattice circulation is zero.

The structure of the paper is as follows. Section 2 presents the governing equations and the dispersion relation for an elastic triangular lattice. Section 3 includes definitions for the dynamic lattice flux and circulation and quantitative evaluations for different dynamic regimes. Wave dispersion versus lattice flux and circulation and the dynamic anisotropy involving lines of zero lattice flux and zero lattice circulation are discussed in Section 4. Finally, we present illustrative examples in Section 5.

2. Governing equations and dispersion. A periodic elastic lattice

The system under consideration is an infinite, periodic triangular array of point masses m, connected by massless elastic links of stiffness c and length l. We assume that the masses are constrained to move in the (x_1x_2)-plane and that their displacements are small. A repetitive cell of the system is shown in Fig. 1a.

In the time-harmonic regime, the governing equations of the periodic triangular lattice can be written in the following matrix form [24]:

$$\left(\boldsymbol{C} - \omega^2 \boldsymbol{M}\right) \boldsymbol{U} = \boldsymbol{0}\,, \tag{1}$$

where ω is the radian frequency, $\boldsymbol{U} = (U_1, U_2)^{\mathrm{T}}$ is the displacement vector and

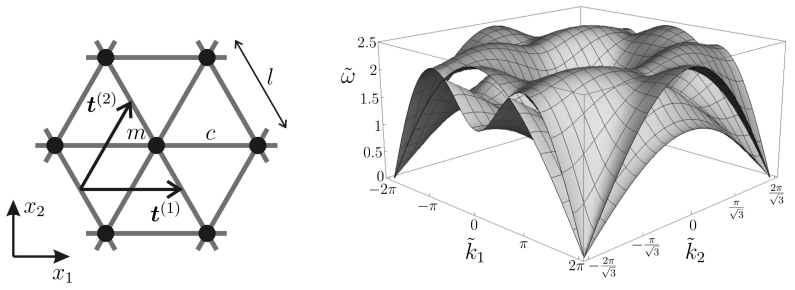

(a) (b)

Figure 1: (a) Periodic cell of the triangular elastic lattice; (b) lower and upper dispersion surfaces of the discrete system.

$\boldsymbol{M} = m\boldsymbol{I}_2$ is the mass matrix, with $\boldsymbol{I}_2$ being the 2×2 identity matrix. Moreover,

$$\boldsymbol{C} = c\begin{pmatrix} 3-2\cos(\zeta l+\xi l)-\frac{1}{2}\left[\cos(\zeta l)+\cos(\xi l)\right] & \frac{\sqrt{3}}{2}\left[\cos(\xi l)-\cos(\zeta l)\right] \\ \frac{\sqrt{3}}{2}\left[\cos(\xi l)-\cos(\zeta l)\right] & 3-\frac{3}{2}\left[\cos(\zeta l)+\cos(\xi l)\right] \end{pmatrix} \tag{2}$$

is the stiffness matrix, where $\boldsymbol{k} = (k_1, k_2)^{\mathrm{T}}$ is the wave vector, $\zeta = k_1/2 + \sqrt{3}k_2/2$ and $\xi = k_1/2 - \sqrt{3}k_2/2$.

In the derivation of Eq. (1), Bloch-Floquet quasi-periodicity conditions have been used, which allow a single repetitive cell to fully characterise the dispersive properties of the infinite system. The Bloch-Floquet conditions account for a phase shift between neighbouring cells and can be expressed by

$$\boldsymbol{U}\left(\boldsymbol{x} + n_1\boldsymbol{t}^{(1)} + n_2\boldsymbol{t}^{(2)}\right) = \boldsymbol{U}(\boldsymbol{x})\,\mathrm{e}^{\mathrm{i}\,\boldsymbol{k}\cdot\boldsymbol{T}\boldsymbol{n}}\,, \tag{3}$$

where $\boldsymbol{x} = (x_1, x_2)^{\mathrm{T}}$ is the position vector, $\boldsymbol{n} = (n_1, n_2)^{\mathrm{T}}$ is the multi-index and $\boldsymbol{T} = \left(\boldsymbol{t}^{(1)}, \boldsymbol{t}^{(2)}\right)$ is the periodicity matrix. The vectors $\boldsymbol{t}^{(1)} = (l, 0)^{\mathrm{T}}$ and $\boldsymbol{t}^{(2)} = \left(l/2, \sqrt{3}\,l/2\right)^{\mathrm{T}}$ are shown in Fig. 1a.

In what follows, we use the normalised quantities

$$\begin{aligned} &\tilde{\boldsymbol{x}} = \boldsymbol{x}/l\,, \quad \tilde{\boldsymbol{U}} = \boldsymbol{U}/l\,, \quad \tilde{\boldsymbol{T}} = \boldsymbol{T}/l\,, \quad \tilde{\boldsymbol{k}} = \boldsymbol{k}\,l\,, \quad \tilde{\zeta} = \zeta\,l\,, \\ &\tilde{\xi} = \xi\,l\,, \quad \tilde{\boldsymbol{M}} = \boldsymbol{M}/m\,, \quad \tilde{\boldsymbol{C}} = \boldsymbol{C}/c\,, \quad \tilde{\omega} = \omega/\sqrt{c/m}\,. \end{aligned} \tag{4}$$

The dispersion relation is obtained by looking for non-trivial solutions of Eq. (1), and it is given by

$$\tilde{\omega}^4 - \mathrm{tr}(\tilde{\boldsymbol{C}})\,\tilde{\omega}^2 + \det(\tilde{\boldsymbol{C}}) = 0\,. \tag{5}$$

The equation above admits two positive solutions:

$$\tilde{\omega}^{(1)}(\tilde{\boldsymbol{k}}) = \sqrt{\frac{\mathrm{tr}(\tilde{\boldsymbol{C}}) - \sqrt{\mathrm{tr}^2(\tilde{\boldsymbol{C}}) - 4\mathrm{det}(\tilde{\boldsymbol{C}})}}{2}}\,, \tag{6a}$$

$$\tilde{\omega}^{(2)}(\tilde{\boldsymbol{k}}) = \sqrt{\frac{\mathrm{tr}(\tilde{\boldsymbol{C}}) + \sqrt{\mathrm{tr}^2(\tilde{\boldsymbol{C}}) - 4\mathrm{det}(\tilde{\boldsymbol{C}})}}{2}}\,. \tag{6b}$$

The two dispersion surfaces of the periodic system are presented in Fig. 1b. We note that the dispersion surfaces meet at six points, called the "Dirac points". The positions of the six Dirac points in the $\tilde{\boldsymbol{k}}$-plane are indicated in Fig. 6 by points D.

After determining the eigenfrequencies $\tilde{\omega}^{(1)} = \tilde{\omega}^{(1)}(\tilde{\boldsymbol{k}})$ and $\tilde{\omega}^{(2)} = \tilde{\omega}^{(2)}(\tilde{\boldsymbol{k}})$, the corresponding eigenvectors (or eigenmodes) $\tilde{\boldsymbol{U}}^{(1)} = \tilde{\boldsymbol{U}}^{(1)}(\tilde{\boldsymbol{k}})$ and $\tilde{\boldsymbol{U}}^{(2)} = \tilde{\boldsymbol{U}}^{(2)}(\tilde{\boldsymbol{k}})$ can be obtained from the vector equations of motion (1), which are re-written below in the form

$$\left\{3 - 2\cos(\tilde{\zeta}+\tilde{\xi}) - \frac{\cos(\tilde{\zeta})+\cos(\tilde{\xi})}{2} - \left(\tilde{\omega}^{(j)}\right)^2\right\}\tilde{U}_1^{(j)} + \left\{\frac{\sqrt{3}\left[\cos(\tilde{\xi})-\cos(\tilde{\zeta})\right]}{2}\right\}\tilde{U}_2^{(j)} = 0\,, \tag{7a}$$

$$\left\{\frac{\sqrt{3}\left[\cos(\tilde{\xi})-\cos(\tilde{\zeta})\right]}{2}\right\}\tilde{U}_1^{(j)} + \left\{3 - \frac{3\left[\cos(\tilde{\zeta})+\cos(\tilde{\xi})\right]}{2} - \left(\tilde{\omega}^{(j)}\right)^2\right\}\tilde{U}_2^{(j)} = 0\,, \tag{7b}$$

with $j = 1, 2$. We note that the eigenvectors corresponding to the lower and upper dispersion surfaces are real and orthogonal.

3. Lattice flux and circulation

In this section, we introduce the discrete definitions of flux and circulation for the lattice described in Section 2. These definitions will be used to characterise the nature of the waves that can propagate in the discrete medium.

3.1. Displacements of the lattice particles

The time-harmonic displacement of a lattice particle for a given eigenmode is obtained by multiplying the eigenvector by the phase shift in time, while the displacements of all the other particles are shifted according to the Bloch-Floquet conditions. If the coordinates of the central node of the lattice unit cell shown in Fig. 1a are identified as $\tilde{\boldsymbol{x}}^0 = (0, 0)$, then the coordinates of the central node of the cell $\boldsymbol{n}$ ($\boldsymbol{n} \in \mathbb{Z}^2$) are given by $\tilde{\boldsymbol{x}}^{(\boldsymbol{n},0)} = \tilde{\boldsymbol{x}}^0 + \tilde{\boldsymbol{T}}\boldsymbol{n}$, where $\tilde{\boldsymbol{T}}$ is the periodicity matrix defined in Section 2. Accordingly, the time-harmonic displacement of a lattice particle for a given eigenmode $j = 1, 2$ is given by

$$\tilde{\boldsymbol{u}}^{(j)}(\tilde{\boldsymbol{x}}, \tilde{t}) = \mathrm{Re}\left(\tilde{\boldsymbol{U}}^{(j)} \mathrm{e}^{\mathrm{i}\left(\tilde{\omega}^{(j)}\tilde{t} - \tilde{\boldsymbol{k}}\cdot\tilde{\boldsymbol{T}}\boldsymbol{n}\right)}\right) = \tilde{\boldsymbol{U}}^{(j)} \cos\left(\tilde{\omega}^{(j)}\tilde{t} - \tilde{\boldsymbol{k}}\cdot\tilde{\boldsymbol{T}}\boldsymbol{n}\right), \tag{8}$$

where time t has been normalised as $\tilde{t} = t\sqrt{c/m}$ and $\tilde{\boldsymbol{U}}^{(j)}$ is a unit vector.

From (8) it is apparent that the trajectory of a generic particle in the lattice is a straight line.

3.2. Definitions of lattice flux and circulation of the discrete displacement vector field

For a triangular lattice considered here, the lattice flux and lattice circulation of the displacement vector $\tilde{\boldsymbol{u}}$ are defined as

$$\tilde{\Phi}_{\tilde{\boldsymbol{u}}} = \mathrm{i}\frac{\sqrt{3}}{2}\,\tilde{\boldsymbol{u}} \cdot \tilde{\boldsymbol{f}} \tag{9}$$

and

$$\tilde{\Gamma}_{\tilde{\boldsymbol{u}}} = -\mathrm{i}\frac{\sqrt{3}}{2}\,\left(\tilde{\boldsymbol{u}} \times \tilde{\boldsymbol{f}}\right) \cdot \boldsymbol{e}_3\,, \tag{10}$$

respectively, where the vector $\tilde{\boldsymbol{f}}$ is given by

$$\tilde{\boldsymbol{f}} = \left(2\sin\left(\tilde{\zeta}+\tilde{\xi}\right) + \sin\left(\tilde{\zeta}\right) + \sin\left(\tilde{\xi}\right),\ \sqrt{3}\,\left[\sin\left(\tilde{\zeta}\right) - \sin\left(\tilde{\xi}\right)\right]\right)^{\mathrm{T}}. \tag{11}$$

Since $\tilde{\boldsymbol{u}}$ is a real time-harmonic quantity (see Eq. (8)), the flux $\tilde{\Phi}_{\tilde{\boldsymbol{u}}}$ and the circulation $\tilde{\Gamma}_{\tilde{\boldsymbol{u}}}$ are pure imaginary time-harmonic quantities. We will derive formulae (9)-(11) in Section 3.2.1.

Since the eigenvectors calculated for the lower and upper dispersion surfaces are real and orthogonal, $\tilde{\Gamma}_{\tilde{\boldsymbol{u}}^{(j)}} = -\mathrm{i}\sqrt{3}/2\,\left(\boldsymbol{e}_3 \times \tilde{\boldsymbol{u}}^{(j)}\right) \cdot \tilde{\boldsymbol{f}} = \mp\mathrm{i}\sqrt{3}/2\,\tilde{\boldsymbol{u}}^{(i)} \cdot \tilde{\boldsymbol{f}} = \mp\tilde{\Phi}_{\tilde{\boldsymbol{u}}^{(i)}}$ (with $i \neq j$). Therefore, the amplitude of the flux of the displacement field determined for one dispersion surface is equal to the amplitude of the circulation of the displacement field calculated for the other surface.

3.2.1. Interpretation of lattice flux and circulation

In a two-dimensional continuum, the flux and circulation of a vector field $\boldsymbol{F}$ are defined by

$$\Phi_{\boldsymbol{F}} = \int_{\partial\Omega} \boldsymbol{F} \cdot \boldsymbol{n}\,\mathrm{d}s \tag{12}$$

and

$$\Gamma_{\boldsymbol{F}} = \int_{\partial\Omega} \boldsymbol{F} \cdot \boldsymbol{t}\,\mathrm{d}s\,, \tag{13}$$

respectively. In the equations above, $\partial\Omega$ is the boundary of the area Ω where the flux and circulation are calculated, $\boldsymbol{n}$ is the outward unit normal vector, $\boldsymbol{t}$ is the unit tangential vector, s is the coordinate that traces the boundary $\partial\Omega$ and $\boldsymbol{e}_3$ is the unit vector perpendicular to the (x_1x_2)-plane and parallel to the x_3-axis.

In order to apply the continuum concepts of flux and circulation to the lattice, which is a discrete system, we consider a generic nodal point of the lattice and its six nearest neighbours. We can denote by Ω the domain inside the hexagon having the six neighbouring points as vertices and by $\partial\Omega$ the boundary of the hexagon (see Fig. 2). We consider the flux and circulation of the normalised displacement vector $\tilde{\boldsymbol{u}}$ defined at the six nodal points. The vectors $\boldsymbol{n}$ and $\boldsymbol{t}$ in (12) and (13) are identified, respectively, as the unit normal vectors and unit tangential vectors to the sides of the hexagon, as illustrated in Fig. 2a and

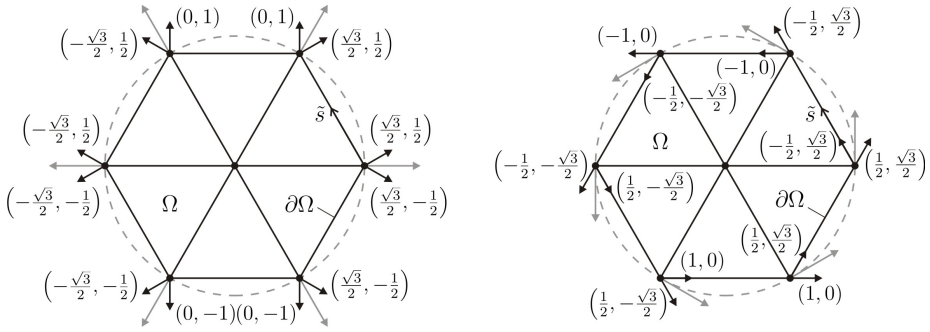

Figure 2: Hexagonal cell, occupying the domain Ω with the boundary $\partial\Omega$, relative to a generic point in the lattice. In (a) the unit normal vectors and in (b) the unit tangential vectors are shown.

in Fig. 2b respectively. We observe that the vector sum of the two unit vectors $\boldsymbol{n}$ (or $\boldsymbol{t}$) at each nodal point is a radial (or tangential) vector with respect to the circle circumscribing the hexagon, shown as a dashed line in Fig. 2a (or Fig. 2b).

Using the Bloch-Floquet conditions (3), the (normalised) flux and circulation of the displacement field are given by

$$\begin{aligned}\tilde{\Phi}_{\tilde{\boldsymbol{u}}} = \int_{\partial\Omega} \tilde{\boldsymbol{u}}\cdot\boldsymbol{n}\,\mathrm{d}\tilde{s} = \frac{1}{2}\Bigg\{&\tilde{\boldsymbol{u}}\mathrm{e}^{\mathrm{i}\tilde{k}_1}\cdot\left(\sqrt{3},0\right)^{\mathrm{T}} + \tilde{\boldsymbol{u}}\mathrm{e}^{-\mathrm{i}\tilde{k}_1}\cdot\left(-\sqrt{3},0\right)^{\mathrm{T}} + \tilde{\boldsymbol{u}}\mathrm{e}^{\mathrm{i}\tilde{\zeta}}\cdot\left(\frac{\sqrt{3}}{2},\frac{3}{2}\right)^{\mathrm{T}}\\ &+\tilde{\boldsymbol{u}}\mathrm{e}^{-\mathrm{i}\tilde{\zeta}}\cdot\left(-\frac{\sqrt{3}}{2},-\frac{3}{2}\right)^{\mathrm{T}} + \tilde{\boldsymbol{u}}\mathrm{e}^{-\mathrm{i}\tilde{\xi}}\cdot\left(-\frac{\sqrt{3}}{2},\frac{3}{2}\right)^{\mathrm{T}} + \tilde{\boldsymbol{u}}\mathrm{e}^{\mathrm{i}\tilde{\xi}}\cdot\left(\frac{\sqrt{3}}{2},-\frac{3}{2}\right)^{\mathrm{T}}\Bigg\}\\ &= \mathrm{i}\frac{\sqrt{3}}{2}\left\{\tilde{u}_1\left[2\sin\left(\tilde{\zeta}+\tilde{\xi}\right)+\sin\left(\tilde{\zeta}\right)+\sin\left(\tilde{\xi}\right)\right]+\tilde{u}_2\sqrt{3}\,\left[\sin\left(\tilde{\zeta}\right)-\sin\left(\tilde{\xi}\right)\right]\right\}\end{aligned} \tag{14}$$

and

$$\begin{aligned}\tilde{\Gamma}_{\tilde{\boldsymbol{u}}} = \int_{\partial\Omega} \tilde{\boldsymbol{u}}\cdot\boldsymbol{t}\,\mathrm{d}\tilde{s} = \frac{1}{2}\Bigg\{&\tilde{\boldsymbol{u}}\mathrm{e}^{\mathrm{i}\tilde{k}_1}\cdot\left(0,\sqrt{3}\right)^{\mathrm{T}} + \tilde{\boldsymbol{u}}\mathrm{e}^{-\mathrm{i}\tilde{k}_1}\cdot\left(0,-\sqrt{3}\right)^{\mathrm{T}} + \tilde{\boldsymbol{u}}\mathrm{e}^{\mathrm{i}\tilde{\zeta}}\cdot\left(-\frac{3}{2},\frac{\sqrt{3}}{2}\right)^{\mathrm{T}}\\ &+\tilde{\boldsymbol{u}}\mathrm{e}^{-\mathrm{i}\tilde{\zeta}}\cdot\left(\frac{3}{2},-\frac{\sqrt{3}}{2}\right)^{\mathrm{T}} + \tilde{\boldsymbol{u}}\mathrm{e}^{-\mathrm{i}\tilde{\xi}}\cdot\left(-\frac{3}{2},-\frac{\sqrt{3}}{2}\right)^{\mathrm{T}} + \tilde{\boldsymbol{u}}\mathrm{e}^{\mathrm{i}\tilde{\xi}}\cdot\left(\frac{3}{2},\frac{\sqrt{3}}{2}\right)^{\mathrm{T}}\Bigg\}\\ &= \mathrm{i}\frac{\sqrt{3}}{2}\left\{-\tilde{u}_1\sqrt{3}\left[\sin\left(\tilde{\zeta}\right)-\sin\left(\tilde{\xi}\right)\right]+\tilde{u}_2\left[2\sin\left(\tilde{\zeta}+\tilde{\xi}\right)+\sin\left(\tilde{\zeta}\right)+\sin\left(\tilde{\xi}\right)\right]\right\},\end{aligned} \tag{15}$$

respectively. In the definitions above, $\tilde{s} = s/l$ is the normalised coordinate. This interpretation is consistent with (9)-(11).

3.2.2. The long wavelength limit

In the long wavelength limit as $\left|\tilde{\boldsymbol{k}}\right| \to 0$, Eqs. (9) and (10) have the following asymptotic approximations:

$$\tilde{\Phi}_{\tilde{\boldsymbol{u}}} \sim \mathrm{i}\tilde{A}_{\mathrm{hex}}\, \tilde{\boldsymbol{u}} \cdot \tilde{\boldsymbol{k}} \qquad \text{for } \left|\tilde{\boldsymbol{k}}\right| \to 0\,, \tag{16}$$

$$\tilde{\Gamma}_{\tilde{\boldsymbol{u}}} \sim -\mathrm{i}\tilde{A}_{\mathrm{hex}} \left(\tilde{\boldsymbol{u}} \times \tilde{\boldsymbol{k}}\right) \cdot \boldsymbol{e}_3 \qquad \text{for } \left|\tilde{\boldsymbol{k}}\right| \to 0\,, \tag{17}$$

where $\tilde{A}_{\mathrm{hex}} = 3\sqrt{3}/2$ is the (normalised) area of the hexagon.

It is apparent from Eqs. (16) and (17) that in the long wavelength limit, where the lattice approximates a continuum, shear and pressure waves are characterised by $\tilde{\Phi}_{\tilde{\boldsymbol{u}}} = 0$ and $\tilde{\Gamma}_{\tilde{\boldsymbol{u}}} = 0$, respectively. For large values of the wave vector, we will distinguish between *flux-free waves* and *circulation-free waves* referring to Eqs. (9) and (10), as the continuum concepts of pressure and shear waves are inappropriate for large $\left|\tilde{\boldsymbol{k}}\right|$.

3.2.3. Properties of the vector $\tilde{\boldsymbol{f}}$

As evident from Eqs. (9) and (10), the vector $\tilde{\boldsymbol{f}}$ plays a key role in the characterisation of waves in a triangular lattice, analogous to the wave vector $\tilde{\boldsymbol{k}}$ in a continuum with respect to flux and circulation.

The components of the vector $\tilde{\boldsymbol{f}}$ are plotted in Fig. 3. For $\tilde{k}_2 = 0$ (part (a)) $\tilde{f}_2 = 0$, while for $\tilde{k}_1 = 0$ (part (b)) $\tilde{f}_1 = 0$. Moreover, we note that for $\tilde{k}_2 = \tilde{k}_1/\sqrt{3}$ (part (c)) $\tilde{f}_2 = \tilde{f}_1/\sqrt{3}$, while for $\tilde{k}_2 = \tilde{k}_1\sqrt{3}$ (part (d)) $\tilde{f}_2 = \tilde{f}_1\sqrt{3}$. The vectors $\tilde{\boldsymbol{f}}$ and $\tilde{\boldsymbol{k}}$ are thus parallel in the directions given by $\arctan\left(\tilde{k}_2/\tilde{k}_1\right) = (n-1)\pi/6$ with $n = 1, .., 12$, and in the neighbourhood of the origin of the $\tilde{\boldsymbol{k}}$-plane where $\tilde{\boldsymbol{f}} \sim 3\tilde{\boldsymbol{k}}$. The relation between vectors $\tilde{\boldsymbol{f}}$ and $\tilde{\boldsymbol{k}}$ is also illustrated in Fig. 3e, where both vectors $\tilde{\boldsymbol{f}}$ and $\tilde{\boldsymbol{k}}$ are plotted in the same diagram.

3.3. Evaluation of lattice flux and circulation using lattice derivatives

The expressions (14) and (15) for lattice flux and lattice circulation, respectively, can also be derived using the notions of divergence and curl of a discrete field. In a continuum, the definitions (12) and (13) for flux and circulation can be written as

$$\Phi_{\boldsymbol{F}} = \int_\Omega \nabla \cdot \boldsymbol{F}\, \mathrm{d}\Omega \tag{18}$$

and

$$\Gamma_{\boldsymbol{F}} = \int_\Omega (\nabla \times \boldsymbol{F}) \cdot \boldsymbol{e}_3\, \mathrm{d}\Omega\,, \tag{19}$$

respectively, using the *divergence theorem* and *Stokes' theorem*. In this section, we show that the definitions of lattice flux and lattice circulation are fully consistent with the notion of lattice derivatives through the discrete forms of divergence theorem and Stokes' theorem.

In order to define the divergence and curl of a vector field in a discrete system, we use the definition of *lattice derivatives* given in [25]. Referring to

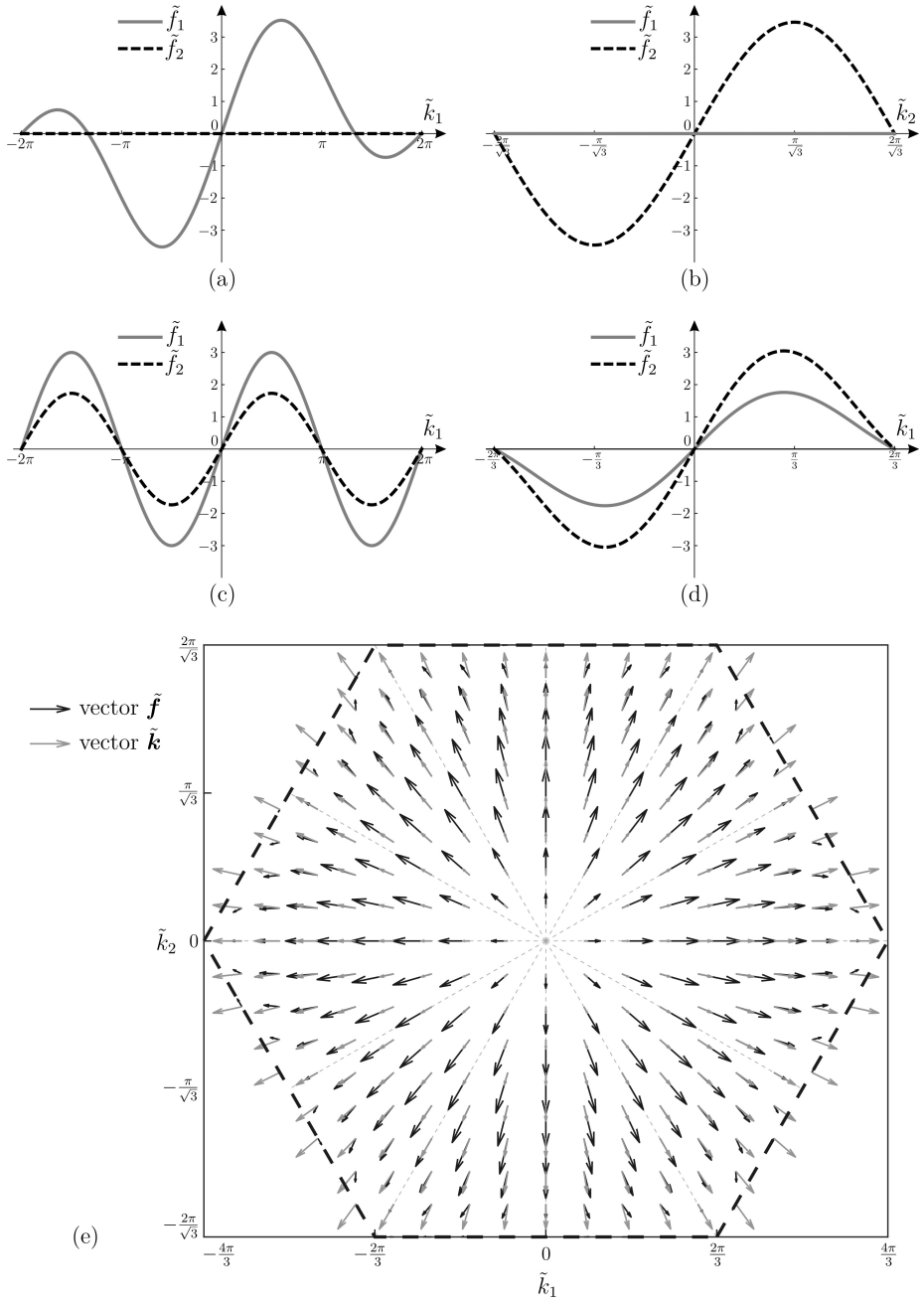

Figure 3: Components of the vector $\tilde{\boldsymbol{f}}$, calculated for $\tilde{k}_2 = 0$ (a), $\tilde{k}_1 = 0$ (b), $\tilde{k}_2 = \tilde{k}_1/\sqrt{3}$ (c), $\tilde{k}_2 = \tilde{k}_1\sqrt{3}$ (d). Vector plots in the $\tilde{\boldsymbol{k}}$-plane of $\tilde{\boldsymbol{f}}$ and $\tilde{\boldsymbol{k}}$ (e).

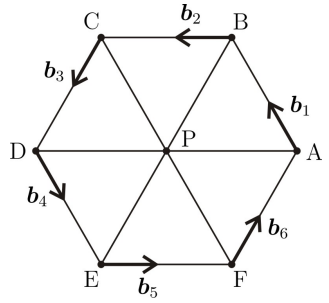

Figure 4: Oriented link vectors for the hexagonal unit cell of the discrete system.

Fig. 4, we denote by $\boldsymbol{b}_j$ ($j = 1, .., 6$) the *oriented link vectors* of the hexagon sides, which are given by

$$\boldsymbol{b}_1 = -\boldsymbol{b}_4 = \left(-\frac{1}{2}, \frac{\sqrt{3}}{2}\right)^{\mathrm{T}}, \boldsymbol{b}_2 = -\boldsymbol{b}_5 = (-1, 0)^{\mathrm{T}}, \boldsymbol{b}_3 = -\boldsymbol{b}_6 = \left(-\frac{1}{2}, -\frac{\sqrt{3}}{2}\right)^{\mathrm{T}}. \tag{20}$$

The (normalised) lattice derivatives associated with the links are then defined as follows:

$$\begin{aligned} &\tilde{\nabla}_1 g = g(\tilde{\boldsymbol{x}}_{\mathrm{B}}) - g(\tilde{\boldsymbol{x}}_{\mathrm{A}}), \ \tilde{\nabla}_2 g = g(\tilde{\boldsymbol{x}}_{\mathrm{C}}) - g(\tilde{\boldsymbol{x}}_{\mathrm{B}}), \ \tilde{\nabla}_3 g = g(\tilde{\boldsymbol{x}}_{\mathrm{D}}) - g(\tilde{\boldsymbol{x}}_{\mathrm{C}}), \\ &\tilde{\nabla}_4 g = g(\tilde{\boldsymbol{x}}_{\mathrm{E}}) - g(\tilde{\boldsymbol{x}}_{\mathrm{D}}), \ \tilde{\nabla}_5 g = g(\tilde{\boldsymbol{x}}_{\mathrm{F}}) - g(\tilde{\boldsymbol{x}}_{\mathrm{E}}), \ \tilde{\nabla}_6 g = g(\tilde{\boldsymbol{x}}_{\mathrm{A}}) - g(\tilde{\boldsymbol{x}}_{\mathrm{F}}), \end{aligned} \tag{21}$$

where g is a generic lattice quantity, that is assumed to satisfy Bloch-Floquet conditions. We note that $\sum_{j=1}^{6} \tilde{\nabla}_j g = 0$. The Cartesian discrete forms $\tilde{\nabla}_{\tilde{x}_1}$ and $\tilde{\nabla}_{\tilde{x}_2}$ of the derivatives $\tilde{\partial}_{\tilde{x}_1}$ and $\tilde{\partial}_{\tilde{x}_2}$ are defined as

$$\begin{aligned} \tilde{\partial}_{\tilde{x}_1} \ &\rightarrow \ \tilde{\nabla}_{\tilde{x}_1} \equiv \frac{2}{6} \sum_{j=1}^{6} (b_1)_j \tilde{\nabla}_j, \\ \tilde{\partial}_{\tilde{x}_2} \ &\rightarrow \ \tilde{\nabla}_{\tilde{x}_2} \equiv \frac{2}{6} \sum_{j=1}^{6} (b_2)_j \tilde{\nabla}_j, \end{aligned} \tag{22}$$

where $(b_1)_j$ and $(b_2)_j$ are the components of $\boldsymbol{b}_j$ in the x_1- and x_2-direction, respectively.

Substituting Eqs. (20) and (21) into (22) and using the Bloch-Floquet conditions (3) for the lattice quantity g, the Cartesian lattice derivatives take the following forms:

$$\begin{aligned} \tilde{\nabla}_{\tilde{x}_1} g &= \frac{\mathrm{i}}{3} \left[2 \sin(\tilde{\zeta} + \tilde{\xi}) + \sin(\tilde{\zeta}) + \sin(\tilde{\xi}) \right], \\ \tilde{\nabla}_{\tilde{x}_2} g &= \frac{\mathrm{i}\sqrt{3}}{3} \left[\sin(\tilde{\zeta}) - \sin(\tilde{\xi}) \right]. \end{aligned} \tag{23}$$

Accordingly, we define the (normalised) lattice divergence and lattice curl of the displacement field $\tilde{\boldsymbol{u}}$ as

$$\begin{aligned}\tilde{\nabla}\cdot\tilde{\boldsymbol{u}} &= \tilde{\nabla}_{\tilde{x}_1}\tilde{u}_1+\tilde{\nabla}_{\tilde{x}_2}\tilde{u}_2\\ &= \frac{\mathrm{i}}{3}\left[2\sin\left(\tilde{\zeta}+\tilde{\xi}\right)+\sin\left(\tilde{\zeta}\right)+\sin\left(\tilde{\xi}\right)\right]\tilde{u}_1+\frac{\mathrm{i}\sqrt{3}}{3}\left[\sin\left(\tilde{\zeta}\right)-\sin\left(\tilde{\xi}\right)\right]\tilde{u}_2\end{aligned} \tag{24}$$

and

$$\begin{aligned}\left(\tilde{\nabla}\times\tilde{\boldsymbol{u}}\right)\cdot\boldsymbol{e}_3 &= \tilde{\nabla}_{\tilde{x}_1}\tilde{u}_2-\tilde{\nabla}_{\tilde{x}_2}\tilde{u}_1\\ &= \frac{\mathrm{i}}{3}\left[2\sin\left(\tilde{\zeta}+\tilde{\xi}\right)+\sin\left(\tilde{\zeta}\right)+\sin\left(\tilde{\xi}\right)\right]\tilde{u}_2-\frac{\mathrm{i}\sqrt{3}}{3}\left[\sin\left(\tilde{\zeta}\right)-\sin\left(\tilde{\xi}\right)\right]\tilde{u}_1\,,\end{aligned} \tag{25}$$

respectively.

Comparing Eqs. (24) and (25) with Eqs. (14) and (15), we notice that the lattice flux $\tilde{\Phi}_{\tilde{\boldsymbol{u}}}$ and the lattice circulation $\tilde{\Gamma}_{\tilde{\boldsymbol{u}}}$ have the form

$$\tilde{\Phi}_{\tilde{\boldsymbol{u}}}=\tilde{A}_{\mathrm{hex}}\,\tilde{\nabla}\cdot\tilde{\boldsymbol{u}}\,,\quad \tilde{\Gamma}_{\tilde{\boldsymbol{u}}}=\tilde{A}_{\mathrm{hex}}\left(\tilde{\nabla}\times\tilde{\boldsymbol{u}}\right)\cdot\boldsymbol{e}_3\,, \tag{26}$$

which is consistent with the continuum definitions of flux and circulation given by (18) and (19), respectively.

4. Wave characterisation in the $\tilde{k}$-plane

As shown in Section 3.1, the trajectories of the lattice particles are straight lines. Generally, these lines are neither parallel nor perpendicular to the vector $\tilde{\boldsymbol{f}}$, defined in (11). This implies that flux and circulation are generally non-zero, according to (9) and (10), for a general mode.

We denote by $\beta^{(j)}$ $(j=1,2)$ the acute angle between the vector $\tilde{\boldsymbol{f}}$ and the displacement $\tilde{\boldsymbol{u}}^{(j)}$, corresponding to the lower $(j=1)$ or upper $(j=2)$ dispersion surface.

In a continuum, the angle between the displacements of the lattice particles and the wave vector $\tilde{\boldsymbol{k}}$ is used to identify the type of waves travelling in the medium. In particular, if this angle is 0 (or $\pi/2$), we refer to pressure (or shear) waves. The discrete medium considered here represents a good approximation of a continuum only when $\left|\tilde{\boldsymbol{k}}\right|\to 0$. In this limit, vectors $\tilde{\boldsymbol{f}}$ and $\tilde{\boldsymbol{k}}$ are parallel, as discussed in Section 3.2.2. This means that $\beta=0$ (or $\beta=\pi/2$) indicates pure pressure (or pure shear) waves. Accordingly, in the long wavelength limit where the discrete medium approximates a continuum, flux-free and circulation-free waves represent shear and pressure waves, respectively.

The displacement vector can be decomposed into a component parallel to the vector $\tilde{\boldsymbol{f}}$, characterised by zero circulation, and a component perpendicular to the vector $\tilde{\boldsymbol{f}}$, for which the flux is zero. When $\beta=0$ (or $\beta=\pi/2$) only the former (or latter) component is different from zero. In this case, waves are

circulation-free (or *flux-free*). We shall see that there are also some special cases where both the flux and circulation are zero. In general, waves in the lattice may be thought as a "mixture" of circulation-free and flux-free waves. This mixture can be characterised by the value of the angle β. Polarisation of elastic waves in continuous media and in crystals is discussed, for example, in [26] and [27], respectively. The notion of polarisation of elastic waves in a chiral lattice is presented in [21].

We indicate by $\tilde{\boldsymbol{u}}_{\mathrm{T}}^{(j)}$ (or $\tilde{\boldsymbol{u}}_{\mathrm{N}}^{(j)}$), where $j = 1, 2$, the component of the displacement vector that is parallel (or perpendicular) to the vector $\tilde{\boldsymbol{f}}$. We emphasise that $\tilde{\Gamma}_{\tilde{\boldsymbol{u}}_{\mathrm{T}}}^{(j)} = 0$ and $\tilde{\Phi}_{\tilde{\boldsymbol{u}}_{\mathrm{N}}}^{(j)} = 0$. Accordingly, the total circulation $\tilde{\Gamma}_{\tilde{\boldsymbol{u}}}^{(j)} = \tilde{\Gamma}_{\tilde{\boldsymbol{u}}_{\mathrm{N}}}^{(j)}$, while the total flux $\tilde{\Phi}_{\tilde{\boldsymbol{u}}}^{(j)} = \tilde{\Phi}_{\tilde{\boldsymbol{u}}_{\mathrm{T}}}^{(j)}$.

As discussed in Section 3.2, flux and circulation vary harmonically in time with the same frequency as the displacement $\tilde{\boldsymbol{u}}$. Flux and circulation differ in phase; however, the phase difference is not relevant for our purposes. Hence it will not be examined in this paper. In what follows, we denote by $|g|$ the amplitude of a generic time-harmonic quantity g.

From Eqs. (9)-(11) we obtain the following expressions for the amplitudes of lattice flux and lattice circulation:

$$\left|\tilde{\Phi}_{\tilde{\boldsymbol{u}}}\right| = \frac{\sqrt{3}}{2}\left|\tilde{\boldsymbol{f}}\right|\cos(\beta)\,, \tag{27a}$$

$$\left|\tilde{\Gamma}_{\tilde{\boldsymbol{u}}}\right| = \frac{\sqrt{3}}{2}\left|\tilde{\boldsymbol{f}}\right|\sin(\beta)\,, \tag{27b}$$

where $\left|\tilde{\boldsymbol{f}}\right| = \sqrt{\tilde{f}_1^2 + \tilde{f}_2^2}$ and β is taken between 0 and $\pi/2$:

$$\beta = \arccos\left(\tilde{\boldsymbol{U}} \cdot \tilde{\boldsymbol{f}} / \left|\tilde{\boldsymbol{f}}\right|\right) \quad \text{if } \tilde{\boldsymbol{U}} \cdot \tilde{\boldsymbol{f}} > 0\,, \tag{28a}$$

$$\beta = \pi - \arccos\left(\tilde{\boldsymbol{U}} \cdot \tilde{\boldsymbol{f}} / \left|\tilde{\boldsymbol{f}}\right|\right) \quad \text{if } \tilde{\boldsymbol{U}} \cdot \tilde{\boldsymbol{f}} < 0\,. \tag{28b}$$

The diagrams of the amplitudes of flux and circulation in the $\tilde{\boldsymbol{k}}$-plane are shown in Figs. 5a and 5b. We note that only two diagrams are presented in Fig. 5 because $\left|\tilde{\Phi}_{\tilde{\boldsymbol{u}}}^{(1)}\right| = \left|\tilde{\Gamma}_{\tilde{\boldsymbol{u}}}^{(2)}\right|$ and $\left|\tilde{\Phi}_{\tilde{\boldsymbol{u}}}^{(2)}\right| = \left|\tilde{\Gamma}_{\tilde{\boldsymbol{u}}}^{(1)}\right|$, as discussed in Section 3.2.

When $\left|\tilde{\boldsymbol{k}}\right| \to 0$, the flux and circulation for both surfaces tend to zero, while the ratios $\left|\tilde{\Phi}_{\tilde{\boldsymbol{u}}}^{(1)}\right| / \left|\tilde{\Gamma}_{\tilde{\boldsymbol{u}}}^{(1)}\right| \to 0$ and $\left|\tilde{\Gamma}_{\tilde{\boldsymbol{u}}}^{(2)}\right| / \left|\tilde{\Phi}_{\tilde{\boldsymbol{u}}}^{(2)}\right| \to 0$. This means that waves associated with the lower dispersion surface are flux-free (or of shear-type in the continuum definition) and those corresponding to the upper dispersion surface are circulation-free (or of pressure-type in the continuum definition). For large values of the wave vector, the flux and the circulation strongly depend on $\tilde{\boldsymbol{k}}$.

Fig. 5c shows how the angles $\beta^{(1)}$ and $\beta^{(2)}$ change with the wave vector $\tilde{\boldsymbol{k}}$. When $\left|\tilde{\boldsymbol{k}}\right| \to 0$, $\beta^{(1)} \to \pi/2$ while $\beta^{(2)} \to 0$. Interestingly, there are 12 directions, given by $\arctan\left(\tilde{k}_2/\tilde{k}_1\right) = (n-1)\pi/6$ with $n = 1, .., 12$, where $\beta^{(1)} = \pi/2$ and

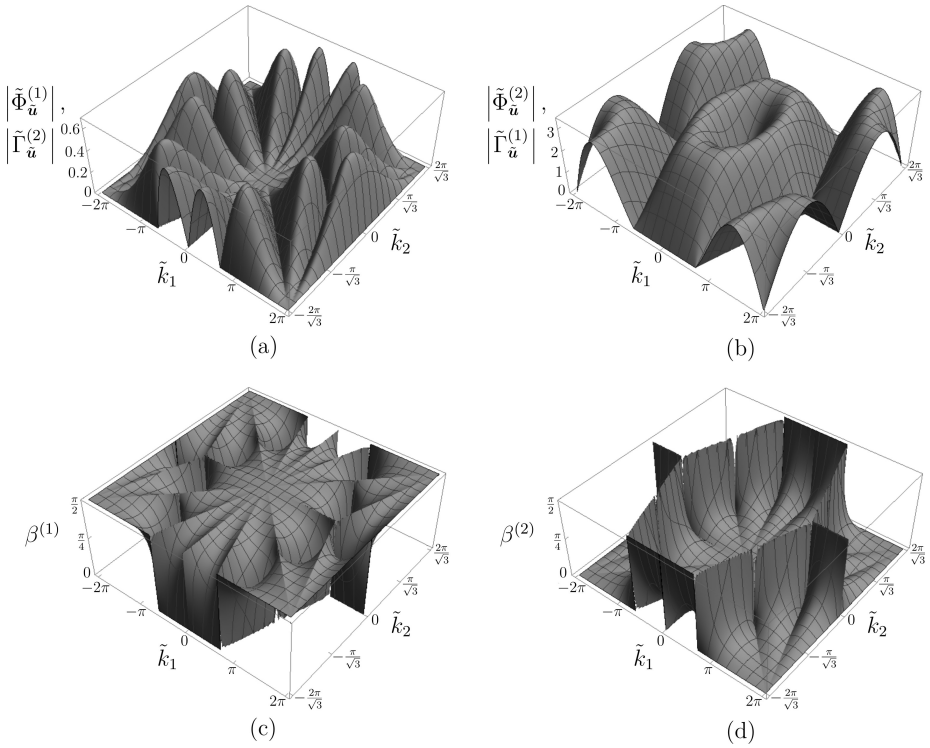

Figure 5: Three-dimensional representations in the $\tilde{\boldsymbol{k}}$-plane of the amplitudes $\left|\tilde{\Phi}^{(1)}_{\tilde{\boldsymbol{u}}}\right| = \left|\tilde{\Gamma}^{(2)}_{\tilde{\boldsymbol{u}}}\right|$ (a) and $\left|\tilde{\Phi}^{(2)}_{\tilde{\boldsymbol{u}}}\right| = \left|\tilde{\Gamma}^{(1)}_{\tilde{\boldsymbol{u}}}\right|$ (b), as well as the angles $\beta^{(1)}$ (c) and $\beta^{(2)}$ (d), calculated in the triangular lattice.

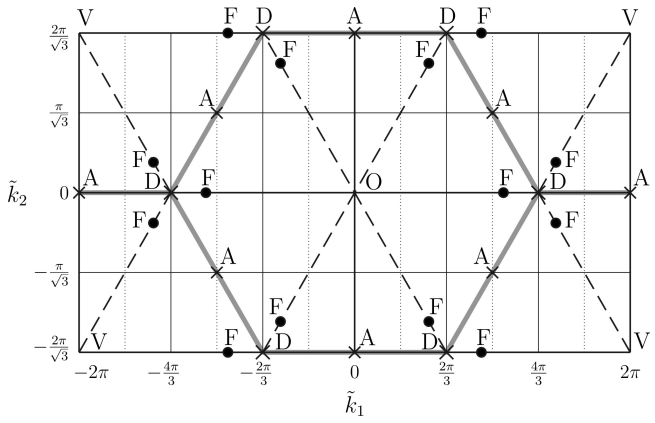

Figure 6: Stationary and Dirac points of the dispersion surfaces, whose properties are given in Tables 1 and 2. The crosses represent stationary points (points A) and Dirac points (points D) for both surfaces, while the dots indicate stationary points (points F) only for the upper surface.

$\beta^{(2)} = 0$. Accordingly, waves characterised by a wave vector falling on one of these lines are either flux-free or circulation-free. This is extremely important, since we maintain "pure" flux-free or circulation-free waves even though the magnitude of the wave vector is not small, as in the long wavelength limit. We also note that $\beta^{(1)} = 0$ and $\beta^{(2)} = \pi/2$ on the sides of the hexagon having its vertices at the six Dirac points of the lattice (see points D in Fig. 6). This hexagon has considerable significance in characterising the nature of wave propagation, as will be seen in the following sections.

We now classify the nature of a propagating wave as a function of its wave vector. There are regions of "pure" flux-free wave propagation, regions of "pure" circulation-free wave propagation and regions where the waves have non-zero flux and circulation. The stationary points of the dispersion surfaces and the hexagon through the Dirac points will be seen to have special significance.

4.1. Stationary points and Dirac points

The stationary and Dirac points of the lower and upper dispersion surfaces are indicated in Fig. 6. Points D denote the Dirac points, which are at the vertices of a hexagon. Points A coincide with the middle points of the hexagon sides. Points A and D are characteristic of both dispersion surfaces, while points F are stationary points only for the upper dispersion surface. The properties of the stationary and Dirac points of the lower (upper) dispersion surface for the triangular lattice are detailed in Table 1 (Table 2).

At the points A and D, both the flux and the circulation are zero for both dispersion surfaces. This is due to the fact that the vector $\tilde{\boldsymbol{f}} = \boldsymbol{0}$ at those points (see also Fig. 3). Furthermore, at the Dirac points D, the coefficients of $\tilde{U}_1$ and $\tilde{U}_2$ in (7) are equal to zero, implying that the eigenvectors can be

Table 1: Stationary points of the lower dispersion surface of the triangular lattice.

Point	$\tilde{k}_1$	$\tilde{k}_2$	$\tilde{\omega}_1$	Type
A	$\pm 2\pi$	0	$\sqrt{2}$	saddle point
	0	$\pm\frac{2\pi}{\sqrt{3}}$		
	$\pm\pi$	$\pm\frac{\pi}{\sqrt{3}}$		
D	$\pm\frac{4\pi}{3}$	0	$\frac{3}{\sqrt{2}}$	maximum
	$\pm\frac{2\pi}{3}$	$\pm\frac{2\pi}{\sqrt{3}}$		

Table 2: Stationary points of the upper dispersion surface of the triangular lattice.

Point	$\tilde{k}_1$	$\tilde{k}_2$	$\tilde{\omega}_2$	Type
A	$\pm 2\pi$	0	$\sqrt{6}$	maximum
	0	$\pm\frac{2\pi}{\sqrt{3}}$		
	$\pm\pi$	$\pm\frac{\pi}{\sqrt{3}}$		
D	$\pm\frac{4\pi}{3}$	0	$\frac{3}{\sqrt{2}}$	minimum
	$\pm\frac{2\pi}{3}$	$\pm\frac{2\pi}{\sqrt{3}}$		
F	$\pm 4\arccos\frac{\sqrt{7}}{4}$	0	$\frac{9}{4}$	saddle point
	$\pm 4\arccos\frac{3}{4}$	$\pm\frac{2\pi}{\sqrt{3}}$		
	$\pm\left[2\pi - \arccos\frac{-1}{8}\right]$	$\pm\left[\frac{2\pi}{\sqrt{3}} - \sqrt{3}\arccos\frac{-1}{8}\right]$		
	$\pm\arccos\frac{-1}{8}$	$\pm\sqrt{3}\arccos\frac{-1}{8}$		

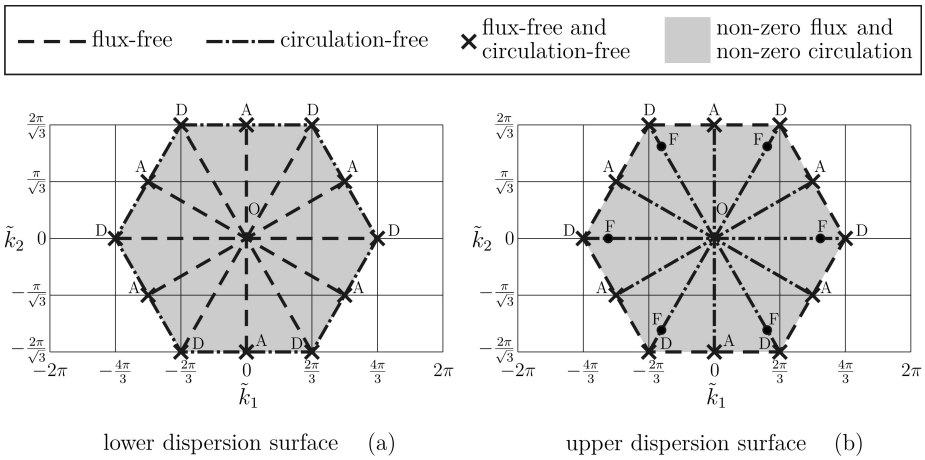

Figure 7: Characterisation of waves in the triangular lattice for the lower dispersion surface (a) and the upper dispersion surface (b).

chosen arbitrarily. This is consistent with the Dirac points being associated with isotropy.

At the points F, which are stationary points only for the upper dispersion surface, $\tilde{\Phi}^{(1)}_{\tilde{\boldsymbol{u}}} = \tilde{\Gamma}^{(2)}_{\tilde{\boldsymbol{u}}} = 0$ while $\tilde{\Phi}^{(2)}_{\tilde{\boldsymbol{u}}} = \tilde{\Gamma}^{(1)}_{\tilde{\boldsymbol{u}}} \neq 0$. This occurs because the points F lie on the radial lines of zero flux for the lower surface and on the radial lines of zero circulation for the upper surface.

4.2. Wave characterisation in the $\tilde{\boldsymbol{k}}$-plane

In Fig. 7 we detail the wave type for any value of the wave vector inside the hexagon passing through the Dirac points for the lower (a) and upper (b) dispersion surface. The diagram is repeated in a doubly periodic array outside the hexagon. The values of $\tilde{\boldsymbol{k}}$ where waves are flux-free or circulation-free are shown as dashed and dot-dashed lines, respectively, while the points where waves are characterised by both zero flux and zero circulation are indicated by crosses. In the grey regions, waves have both non-zero flux-free and non-zero circulation-free components.

We observe that the crosses, where both the flux and the circulation are zero, are at the intersections between the dashed and dot-dashed lines, where either the flux or the circulation is zero.

4.2.1. Lines of zero flux or zero circulation

In what follows, we give the analytical description of the results presented in Fig. 7.

Eq. (1) can be written in normalised form as

$$\tilde{\boldsymbol{B}}\tilde{\boldsymbol{U}} = \begin{pmatrix} \tilde{B}_{11} & \tilde{B}_{12} \\ \\ \tilde{B}_{21} & \tilde{B}_{22} \end{pmatrix} \begin{pmatrix} \tilde{U}_1 \\ \\ \tilde{U}_2 \end{pmatrix} = \boldsymbol{0} \qquad \text{with} \quad \tilde{\boldsymbol{B}} = \tilde{\boldsymbol{C}} - \tilde{\omega}^2 \tilde{\boldsymbol{M}}\,, \tag{29}$$

that leads to $\tilde{U}_1 = -\tilde{B}_{12}\tilde{U}_2/\tilde{B}_{11}$ if $\tilde{B}_{11} \neq 0$ or $\tilde{U}_2 = -\tilde{B}_{21}\tilde{U}_1/\tilde{B}_{22}$ if $\tilde{B}_{22} \neq 0$. According to (9) and (29), flux is zero if one of the following conditions is met:

$$\tilde{B}_{11}\tilde{f}_2 = \tilde{B}_{12}\tilde{f}_1 \qquad \text{if} \quad \tilde{B}_{11} \neq 0\,; \tag{30a}$$

$$\tilde{B}_{21}\tilde{f}_2 = \tilde{B}_{22}\tilde{f}_1 \qquad \text{if} \quad \tilde{B}_{22} \neq 0\,. \tag{30b}$$

We note that $\tilde{B}_{11} = \tilde{B}_{11}(\tilde{\omega})$ and $\tilde{B}_{22} = \tilde{B}_{22}(\tilde{\omega})$, while $\tilde{B}_{12}$, $\tilde{B}_{21}$, $\tilde{f}_1$, $\tilde{f}_2$ are independent of $\tilde{\omega}$.

We start by proving that $\tilde{\Phi}^{(2)}_{\tilde{\boldsymbol{u}}} = 0$ in the hexagon passing through the Dirac points. The left-hand side and right-hand side terms of (30a) are given by

$$\begin{aligned} \tilde{B}_{11}(\tilde{\omega}^{(2)})\tilde{f}_2 = \sqrt{3}\cos\left(\frac{\tilde{k}_1}{2}\right)\sin\left(\frac{\sqrt{3}\tilde{k}_2}{2}\right)\Bigg[2\cos\left(\frac{\tilde{k}_1}{2}\right)\cos\left(\frac{\sqrt{3}\tilde{k}_2}{2}\right) \\ - 2\cos\left(\tilde{k}_1\right) - \sqrt{2}\Bigg\{3 - \cos\left(\tilde{k}_1\right) + \cos\left(2\tilde{k}_1\right) + \Big[2\cos\left(\tilde{k}_1\right) - 1\Big]\cos\left(\sqrt{3}\tilde{k}_2\right) \\ -2\left[\cos\left(\frac{\tilde{k}_1}{2}\right) + \cos\left(\frac{3\tilde{k}_1}{2}\right)\right]\cos\left(\frac{\sqrt{3}\tilde{k}_2}{2}\right)\Bigg\}^{1/2}\Bigg] \end{aligned} \tag{31}$$

and

$$\tilde{B}_{12}\tilde{f}_1 = 2\sqrt{3}\left[2\cos\left(\frac{\tilde{k}_1}{2}\right) + \cos\left(\frac{\sqrt{3}\tilde{k}_2}{2}\right)\right]\sin^2\left(\frac{\tilde{k}_1}{2}\right)\sin\left(\frac{\sqrt{3}\tilde{k}_2}{2}\right), \tag{32}$$

respectively. We will investigate the horizontal and inclined lines of the hexagon separately.

- $\underline{\tilde{k}_2 = (2n+1)2\pi/\sqrt{3}\ (n \in \mathbb{Z})}$. The equation in (30a) is clearly satisfied since here $\sin\left(\sqrt{3}\tilde{k}_2/2\right) = 0$. However,

$$\tilde{B}_{11}(\tilde{\omega}^{(2)}) = \begin{cases} -2\left[\cos\left(\frac{\tilde{k}_1}{2}\right) + \cos\left(\tilde{k}_1\right)\right] & \text{if } -\frac{2\pi}{3} + 4n\pi \leq \tilde{k}_1 \leq \frac{2\pi}{3} + 4n\pi\,, \\ 0 & \text{otherwise}\,. \end{cases} \tag{33}$$

  Hence, (30a) is valid only on the horizontal sides of the hexagons connecting the Dirac points of the lattice. For $\frac{2\pi}{3} + 4n\pi \leq \tilde{k}_1 \leq \frac{10\pi}{3} + 4n\pi$, $\tilde{B}_{22}(\tilde{\omega}^{(2)}) \neq 0$, but (30b) is not satisfied.

- $\underline{\tilde{k}_2 = \pm\sqrt{3}\tilde{k}_1 + (2n+1)4\pi/\sqrt{3}\ (n \in \mathbb{Z})}$. In this case, Eqs. (31) and (32) become

$$\tilde{B}_{11}(\tilde{\omega}^{(2)})\tilde{f}_2 = \mp 2\sqrt{3}\cos\left(\frac{\tilde{k}_1}{2}\right)\sin^2\left(\frac{\tilde{k}_1}{2}\right)\sin\left(\frac{3\tilde{k}_1}{2}\right)\left[1 + 2\cos\left(\tilde{k}_1\right) + \left|2 + 4\cos\left(\tilde{k}_1\right)\right|\right] \tag{34}$$

and

$$\tilde{B}_{12}\tilde{f}_1 = \pm\sqrt{3}\csc\left(\tilde{k}_1\right)\sin^2\left(\frac{\tilde{k}_1}{2}\right)\left[\sin\left(\tilde{k}_1\right) + \sin\left(2\tilde{k}_1\right)\right]^2 , \tag{35}$$

respectively. Formulae (34) and (35) are identical for $\frac{2\pi}{3} + 2n\pi \leq \tilde{k}_1 \leq \frac{4\pi}{3} + 2n\pi$, namely at the inclined sides of the hexagons passing through the Dirac points. We also point out that

$$\tilde{B}_{11}(\tilde{\omega}^{(2)}) = -\sin^2\left(\frac{\tilde{k}_1}{2}\right)\left[1 + 2\cos\left(\tilde{k}_1\right) + \left|2 + 4\cos\left(\tilde{k}_1\right)\right|\right] , \tag{36}$$

which is zero only in a countable set of points of the $\tilde{\boldsymbol{k}}$-plane.

Next, we focus on the 12 directions passing through the origin of the $\tilde{\boldsymbol{k}}$-plane, given by $\arctan\left(\tilde{k}_2/\tilde{k}_1\right) = (n-1)\pi/6$ $(n = 1, .., 12)$. We want to prove that $\tilde{\Phi}^{(1)}_{\tilde{\boldsymbol{u}}} = 0$ along these lines. For $\tilde{\omega} = \tilde{\omega}^{(1)}$, the right-hand side of (30a) is the same as in (32), while the left-hand side of (30a) is given by

$$\begin{aligned}\tilde{B}_{11}(\tilde{\omega}^{(1)})\tilde{f}_2 = \sqrt{3}\cos\left(\frac{\tilde{k}_1}{2}\right)\sin\left(\frac{\sqrt{3}\tilde{k}_2}{2}\right)\Bigg[&2\cos\left(\frac{\tilde{k}_1}{2}\right)\cos\left(\frac{\sqrt{3}\tilde{k}_2}{2}\right) \\ &- 2\cos\left(\tilde{k}_1\right) + \sqrt{2}\Bigg\{3 - \cos\left(\tilde{k}_1\right) + \cos\left(2\tilde{k}_1\right) + \left[2\cos\left(\tilde{k}_1\right) - 1\right]\cos\left(\sqrt{3}\tilde{k}_2\right) \\ &-2\left[\cos\left(\frac{\tilde{k}_1}{2}\right) + \cos\left(\frac{3\tilde{k}_1}{2}\right)\right]\cos\left(\frac{\sqrt{3}\tilde{k}_2}{2}\right)\Bigg\}^{1/2}\Bigg]\end{aligned} \tag{37}$$

- $\underline{\tilde{k}_2 = n4\pi/\sqrt{3}\ (n \in \mathbb{Z})}$. The equation in (30a) is clearly satisfied, because both (31) and (32) are zero considering that on these lines $\sin\left(\sqrt{3}\tilde{k}_2/2\right) = 0$. Since

$$\tilde{B}_{11}(\tilde{\omega}^{(1)}) = \begin{cases} 2\left[\cos\left(\frac{\tilde{k}_1}{2}\right) - \cos\left(\tilde{k}_1\right)\right] & \text{if } -\frac{4\pi}{3} + 4n\pi \leq \tilde{k}_1 \leq \frac{4\pi}{3} + 4n\pi\,, \\ 0 & \text{otherwise}\,, \end{cases} \tag{38}$$

the relation (30a) is valid only inside the hexagons, as shown in Fig. 7. In the ranges of $\tilde{k}_1$ where $\tilde{B}_{11}(\tilde{\omega}^{(1)}) = 0$, the relation (30b) is not satisfied.

- $\underline{\tilde{k}_1 = n4\pi\ (n \in \mathbb{Z})}$. $\tilde{B}_{11}(\tilde{\omega}^{(1)}) = 0$, hence relation (30a) cannot be used. However, relation (30b) is satisfied, because $\tilde{B}_{21} = 0$, $\tilde{f}_1 = 0$ and

$$\tilde{B}_{22}(\tilde{\omega}^{(1)}) = 2 - 2\cos\left(\frac{\sqrt{3}\tilde{k}_2}{2}\right) , \tag{39}$$

which is zero only in a countable set of points.

- $\tilde{k}_2 = \pm\tilde{k}_1/\sqrt{3} + n4\pi/\sqrt{3}$ $(n \in \mathbb{Z})$. In this case, Eq. (30a) is satisfied everywhere apart from a countable set of points. In particular,

$$\tilde{B}_{11}(\tilde{\omega}^{(1)})\tilde{f}_2 = \tilde{B}_{12}\tilde{f}_1 = \pm 3\sqrt{3}\sin^2\left(\frac{\tilde{k}_1}{2}\right)\sin(\tilde{k}_1) \tag{40}$$

and

$$\tilde{B}_{11}(\tilde{\omega}^{(1)}) = 3\sin^2\left(\frac{\tilde{k}_1}{2}\right). \tag{41}$$

- $\tilde{k}_2 = \pm\sqrt{3}\tilde{k}_1 + n4\pi/\sqrt{3}$ $(n \in \mathbb{Z})$. Along these lines, the left-hand side and right-hand side terms of (30a) are given by

$$\tilde{B}_{11}(\tilde{\omega}^{(1)})\tilde{f}_2 = \mp\sqrt{3}\left[1 + 2\cos(\tilde{k}_1) - \left|2 + 4\cos(\tilde{k}_1)\right|\right]\sin^2\left(\frac{\tilde{k}_1}{2}\right)\left[\sin(\tilde{k}_1) + \sin(2\tilde{k}_1)\right] \tag{42}$$

and

$$\tilde{B}_{12}\tilde{f}_1 = \pm\sqrt{3}\csc(\tilde{k}_1)\sin^2\left(\frac{\tilde{k}_1}{2}\right)\left[\sin(\tilde{k}_1) + \sin(2\tilde{k}_1)\right]^2, \tag{43}$$

respectively. The last two formulae are equivalent if $-2\pi/3 + 2n\pi \leq \tilde{k}_1 \leq 2\pi/3 + 2n\pi$. In this case,

$$\tilde{B}_{11}(\tilde{\omega}^{(1)}) = \frac{1}{2}\left\{2\left|\cos(\tilde{k}_1) - \cos(2\tilde{k}_1)\right| - \left[\cos(\tilde{k}_1) - \cos(2\tilde{k}_1)\right]\right\}, \tag{44}$$

which is not zero except in a countable set of points.

5. Illustrative examples

Here, we show how waves with specific values of the wave vector $\tilde{\boldsymbol{k}}$ propagate in the triangular lattice.

We start by considering a large value of $\left|\tilde{\boldsymbol{k}}\right|$, in particular $\tilde{k}_1 = 2.15$ and $\tilde{k}_2 = 3.19$. This wave vector lies in one of the grey regions of Fig. 7, characterised by "mixed" non-zero flux-free and non-zero circulation-free components. The corresponding frequencies in the lower and upper dispersion surface are $\tilde{\omega}^{(1)} = 1.96$ and $\tilde{\omega}^{(2)} = 2.24$, respectively. The components of the vector $\tilde{\boldsymbol{f}}$ are given by $\tilde{f}_1 = 0.04$ and $\tilde{f}_2 = 0.61$. Using (27), we derive the amplitudes of flux and circulation, namely $\left|\tilde{\Phi}^{(1)}_{\tilde{\boldsymbol{u}}}\right| = \left|\tilde{\Gamma}^{(2)}_{\tilde{\boldsymbol{u}}}\right| = 0.386$ and $\left|\tilde{\Phi}^{(2)}_{\tilde{\boldsymbol{u}}}\right| = \left|\tilde{\Gamma}^{(1)}_{\tilde{\boldsymbol{u}}}\right| = 0.366$. The angles between the vector $\tilde{\boldsymbol{f}}$ and the straight-line trajectories of the particles for the two dispersion surfaces are $\beta^{(1)} = 0.76$ rad and $\beta^{(2)} = 0.81$ rad. The trajectory of a lattice particle calculated for the lower (upper) dispersion surface is shown in Fig. 8 by a dashed (dot-dashed) line. We point out that the two trajectories are perpendicular to each other, because the corresponding eigenvectors are orthogonal.

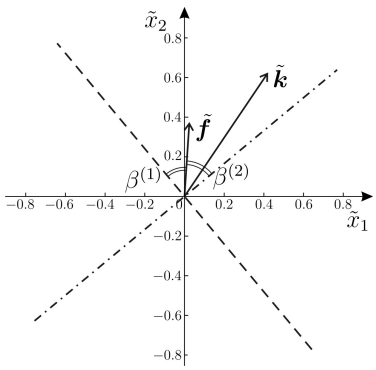

Figure 8: Trajectory of a generic particle in the lattice corresponding to the lower (dashed line) and upper (dot-dashed line) dispersion surface, determined for $\tilde{k}_1 = 2.15$ and $\tilde{k}_2 = 3.19$. The wave vector $\tilde{\boldsymbol{k}}$, the vector $\tilde{\boldsymbol{f}}$ and the angles $\beta^{(j)}$ are also plotted in the figures.

The motions of the particles in the lattice for the two dispersion surfaces, both calculated for $\tilde{k}_1 = 2.15$ and $\tilde{k}_2 = 3.19$, are shown in the videos included in the Supplementary Material (see [28]). The total displacements and the components of the displacements tangential to $\tilde{\boldsymbol{f}}$ and normal to $\tilde{\boldsymbol{f}}$ are displayed in the videos. The magenta and green arrows represent the wave vector $\tilde{\boldsymbol{k}}$ and the vector $\tilde{\boldsymbol{f}}$, respectively. Video1a-Video1f illustrate that the total motion of each lattice particle is the superposition of a flux-free and a circulation-free component.

For a smaller value of the wave vector, say $\tilde{k}_1 = 0.20$ and $\tilde{k}_2 = 0.30$, the lattice approximates a continuum. In this case, the vectors $\tilde{\boldsymbol{k}}$ and $\tilde{\boldsymbol{f}}$ are parallel to each other. The motion is of shear (or pressure) type in the lower (or upper) dispersion surface. Accordingly, the tangential (or normal) component of the displacement vector is very small (see Video2a-Video2f in the Supplementary Material [28]).

In Video3a-Video3f, the wave vector $\left(\tilde{k}_1, \tilde{k}_2\right)^{\mathrm{T}} = (2.15, 1.24)^{\mathrm{T}}$, which is on the line inclined by 30° with respect to the $\tilde{k}_1$-axis. Although the modulus of the wave vector is large, the lattice motions corresponding to the lower and upper surfaces are similar to those observed in Video2a-Video2f for a small wave vector. The reason is that on the line $\tilde{k}_1/\tilde{k}_2 = \sqrt{3}$ the flux (or circulation) is zero in the lower (or upper) surface, as shown in Fig. 7a (or Fig. 7b), hence the tangential (or normal) component to $\tilde{\boldsymbol{f}}$ is null.

We note that flux-free waves in Video2a represent the case of small $\left|\tilde{\boldsymbol{k}}\right|$ and hence are similar to shear waves in a continuum. On the other hand, in Video3a, which also illustrates flux-free waves, the wavelength is comparable to the size of the elementary cell and $\left|\tilde{\boldsymbol{k}}\right|$ is finite. Similar observations apply to circulation-free waves, shown in Video2d and Video3d for small and finite values of $\left|\tilde{\boldsymbol{k}}\right|$, respectively.

Video4a-Video4f show the lattice motion at the stationary point A with coordinates $\tilde{k}_1 = \pi$ and $\tilde{k}_2 = \pi/\sqrt{3}$ (see Fig. 6 and Table 1). Standing waves are clearly visible from the videos. In addition, we note that the tangential (normal) component of the displacement is zero in the lower (upper) dispersion surface, because $\beta^{(1)} = \pi/2$ rad ($\beta^{(2)} = 0$ rad).

Finally, Video5a-Video5f present the motion of the lattice particles when the wave vector is on the hexagon connecting the Dirac points, shown in Fig. 6. For the calculations, we have taken $\tilde{k}_1 = 3.67$ and $\tilde{k}_2 = 0.91$. In this case, the normal (tangential) component of the displacement is equal to zero in the lower (upper) dispersion surface, since $\beta^{(1)} = 0$ rad ($\beta^{(2)} = \pi/2$ rad).

6. Conclusions

The paper has addressed a fundamental issue of quantitative and graphical characterisation of the dynamic anisotropy of waves in a vector elastic lattice. Compared to the earlier work [21], which discussed wave polarisation in elastic structured media, an additional viewpoint has been proposed and fully implemented to take into account effects of pressure and shear in the dynamic elastic lattice. Although in the long-wave regime corresponding to a continuum approximation the matter appears to be straightforward, additional lattice constraints make coupling complex in the intermediate and high frequency regimes.

In particular, we have identified quantitative characteristics of waveforms in an elastic lattice to generalise the notion of pressure and shear waves used in the continuum. The cases of high frequency and wavelength comparable to the size of the elementary cell are considered in detail. These include dynamic anisotropy and dynamic neutrality in the context of waveforms classified by the lattice flux and lattice circulation attributed to them.

Acknowledgements

The authors would like to thank the EPSRC (UK) for its support through Programme Grant no. EP/L024926/1.

References

[1] Barenblatt G.I., 1987. *Dimensional Analysis*. Gordon and Breach Science Publishers, New York, London, Paris.

[2] Barenblatt G.I., 1996. *Scaling, Self-similarity, and Intermediate Asymptotics*. Cambridge University Press, Cambridge.

[3] Barenblatt G.I., 2003. *Scaling*. Cambridge University Press, Cambridge.

[4] Barenblatt G.I., 2014. *Flow, Deformation and Fracture*. Cambridge University Press, Cambridge.

[5] Slepyan L.I., 2002. *Models and Phenomena in Fracture Mechanics*. Springer, Berlin.

[6] Slepyan L.I., Movchan A.B., Mishuris G.S., 2010. Crack in a lattice waveguide. *Int. J. Fract.* **162**, 91-106. (doi: 10.1007/s10704-009-9389-5)

[7] Nieves M.J., Mishuris G.S., Slepyan L.I., 2016. Analysis of dynamic damage propagation in discrete beam structures. *Int. J. Solids Struct.* **97-98**, 699-713. (doi: 10.1016/j.ijsolstr.2016.02.033)

[8] Nieves M.J., Mishuris G.S., Slepyan L.I., 2017. Transient wave in a transformable periodic flexural structure. *Int. J. Solids Struct.* **112**, 185-208. (doi: 10.1016/j.ijsolstr.2016.11.012)

[9] Bensoussan A., Lions J.L., Papanicolaou G., 1978. *Asymptotic Analysis for Periodic Structures*. North-Holland, Amsterdam.

[10] Bakhvalov N.S., Panasenko G.P., 1984. *Homogenization: Averaging Processes in Periodic Media*. Mathematics and Its Applications (Soviet Series), vol. 36, Kluwer Academic Publishers, Dordrecht-Boston-London.

[11] Zhikov V.V., Kozlov S.M., Oleinik O.A., 1994. *Homogenization of Differential Operators and Integral Functionals*. Springer, Heidelberg.

[12] Panasenko G.P., 2005. *Multi-scale Modelling for Structures and Composites*. Springer, Dordrecht.

[13] Craster R.V., Kaplunov J., Postnova J., 2010. High-frequency asymptotics, homogenisation and localisation for lattices. *Q. J. Mech. Appl. Math.* **63**, 497-519. (doi: 10.1093/qjmam/hbq015)

[14] Antonakakis T., Craster R.V., Guenneau S., 2014. Homogenisation for elastic photonic crystals and dynamic anisotropy. *J. Mech. Phys. Solids* **71**, 84-96. (doi: 10.1016/j.jmps.2014.06.006)

[15] Colquitt D.J., Craster R.V., Makwana M., 2015. High frequency homogenisation for elastic lattices. *Q. J. Mech. Appl. Math.* **68**, 203-230. (doi: 10.1093/qjmam/hbv005)

[16] Ayzenberg-Stepanenko M., Slepyan L.I., 2008. Resonant-frequency primitive waveforms and star waves in lattices. *J. Sound Vib.* **313**, 812-821. (doi: 10.1016/j.jsv.2007.11.047)

[17] Colquitt D.J., Jones I.S., Movchan N.V., Movchan A.B., McPhedran R.C., 2012. Dynamic anisotropy and localization in elastic lattice systems. *Waves Random Complex Media* **22**, 143-159. (doi: 10.1080/17455030.2011.633940)

[18] Movchan A.B., Slepyan L.I., 2014. Resonant waves in elastic structured media: Dynamic homogenisation versus Green's functions. *Int. J. Solids Struct.* **51**, 2254-2260. (doi: 10.1016/j.ijsolstr.2014.03.015)

[19] Brun M., Movchan A.B., Movchan N.V., 2010. Shear polarisation of elastic waves by a structured interface. *Continuum Mech. Thermodyn.* **22**, 663-677. (doi: 10.1007/s00161-010-0143-z)

[20] Brun M., Jones I.S., Movchan A.B., 2012. Vortex-type elastic structured media and dynamic shielding. *Proc. R. Soc. A* **468**, 3027-3046. (doi: 10.1098/rspa.2012.0165)

[21] Carta G., Brun M., Movchan A.B., Movchan N.V., Jones I.S., 2014. Dispersion properties of vortex-type monatomic lattices. *Int. J. Solids Struct.* **51**, 2213-2225. (doi: 10.1016/j.ijsolstr.2014.02.026)

[22] Carta G., Jones I.S., Movchan N.V., Movchan A.B., Nieves M.J., 2017. "Deflecting elastic prism" and unidirectional localisation for waves in chiral elastic systems. *Sci. Rep.* **7**, 26. (doi: 10.1038/s41598-017-00054-6)

[23] Garau M., Carta G., Nieves M.J., Jones I.S., Movchan N.V., Movchan A.B., 2018. Interfacial waveforms in chiral lattices with gyroscopic spinners. *Proc. R. Soc. London A* **474**, 20180132. (doi: 10.1098/rspa.2018.0132)

[24] Martinsson P.G., Movchan A.B., 2003. Vibrations of lattice structures and phononic band gaps. *Q. J. Mech. Appl. Math.* **56**, 45-64. (doi: 10.1093/qjmam/56.1.45)

[25] Dietel J., Kleinert H., 2006. Triangular lattice model of two-dimensional defect melting. *Phys. Rev. B* **73**, 024113. (doi: 10.1103/PhysRevB.73.024113)

[26] Achenbach J.D., 1973. *Wave Propagation in Elastic Solids*. North-Holland Publishing Company, Amsterdam, London.

[27] Musgrave M.J.P., 1970. *Crystal Acoustics*. Holden-Day, San Francisco.

[28] Carta G., Jones I.S., Movchan N.V., Movchan A.B., 2018. Waveforms - video file repository. Link: *https://www.dropbox.com/sh/ae2n3ggsiq2ju21/AAAYJiS1N4JCBNjGFR-4LyyKa?dl=0*.